Structure
Article

Crystal Structure of the Pestivirus Envelope Glycoprotein E^{rns} and Mechanistic Analysis of Its Ribonuclease Activity

Thomas Krey,[1,2,*] Francois Bontems,[1,2,3] Clemens Vonrhein,[4] Marie-Christine Vaney,[1,2] Gerard Bricogne,[4] Till Rümenapf,[5] and Félix A. Rey[1,2,*]
[1]Unité de Virologie Structurale, Institut Pasteur, 75015 Paris, France
[2]CNRS URA 3015, Virologie, 75015 Paris, France
[3]CNRS UPR 2301, Chimie et Biologie Structurales, Institut de Chimie des Substances Naturelles, Gif-sur-Yvette, France
[4]Global Phasing Ltd., Sheraton House, Castle Park, Cambridge CB3 0AX, UK
[5]Institut für Virologie, Justus-Liebig-Universität, 35390 Giessen, Germany
*Correspondence: tkrey@pasteur.fr (T.K.), rey@pasteur.fr (F.A.R.)
DOI 10.1016/j.str.2012.03.018

SUMMARY

Pestiviruses, which belong to the *Flaviviridae* family of RNA viruses, are important agents of veterinary diseases causing substantial economical losses in animal farming worldwide. Pestivirus particles display three envelope glycoproteins at their surface: E^{rns}, E1, and E2. We report here the crystal structure of the catalytic domain of E^{rns}, the ribonucleolytic activity of which is believed to counteract the innate immunity of the host. The structure reveals a three-dimensional fold corresponding to T2 ribonucleases from plants and fungi. Cocrystallization experiments with mono- and oligonucleotides revealed the structural basis for substrate recognition at two binding sites previously identified for T2 RNases. A detailed analysis of poly-U cleavage products using ^{31}P-NMR and size exclusion chromatography, together with molecular docking studies, provides a comprehensive mechanistic picture of E^{rns} activity on its substrates and reveals the presence of at least one additional nucleotide binding site.

INTRODUCTION

Pestiviruses include important pathogens of veterinary concern, such as the bovine viral diarrhea virus (BVDV) and the classical swine fever virus (CSFV). They constitute a separate genus in the *Flaviviridae* family of enveloped, positive-sense, single-stranded RNA viruses, together with the *Flavivirus* and *Hepacivirus* genera. The pestivirus genome consists of an RNA molecule of about 12,300 nucleotides, containing a single open reading frame that codes for a single polyprotein precursor of ~3900 amino acids. The N-terminal third of this precursor contains the structural proteins C (Core protein), and glycoproteins E^{rns}, E1, and E2 (Lindenbach et al., 2007; E^{rns} is the abbreviation of envelope protein RNase secreted). All three glycoproteins were found to be present in the viral envelope as disulfide-linked homo- and heterodimers (Durantel et al., 2001; Lazar et al., 2003; Thiel et al., 1991; Weiland et al., 1990). While the glycoproteins E1 and E2 have their counterparts in other members of the *Flaviviridae* family, E^{rns} is unique to the pestivirus genus (Lindenbach et al., 2007). It is essential for production of infectious viral particles and is targeted by neutralizing antibodies (Weiland et al., 1992; Windisch et al., 1996). E^{rns} was also shown to play a role in virus attachment to cells via a positively charged amino acid stretch that has been suggested to interact with glycosaminoglycans such as heparan sulfate (Hulst et al., 2001; Iqbal et al., 2000; Iqbal and McCauley, 2002). Nevertheless, E^{rns} is dispensable for viral entry, as shown by the infectivity of retrovirus particles pseudotyped with glycoproteins E1 and E2 (Wang et al., 2004).

E^{rns} has ribonucleolytic activity on single- and double-stranded RNA (Iqbal et al., 2004) and has been classified within the T2 ribonuclease (RNase) family (Schneider et al., 1993). Enzymes from this family have been identified in protozoans, plants, bacteria, animals, and pestiviruses (reviewed in Deshpande and Shankar, 2002). T2 RNases exert their highest activity in an acidic environment (pH 3.5–6.5), in keeping with their cellular localization within acidic organelles like lysosomes or the vacuole (Deshpande and Shankar, 2002). Several biological functions of T2 RNases—both dependent and independent on the catalytic activity—have been identified, including breakdown of self-RNA, scavenging of nucleic acids and/or phosphate, intra- and extracellular cytotoxicity, and modulation of the host immune system (Luhtala and Parker, 2010). T2 RNases are mostly monomeric glycosylated proteins (20–40 kDa) with no strict substrate specificity, although individual RNases have been reported to preferentially cleave downstream of adenine (Deshpande and Shankar, 2002). Substrate binding of T2 RNases is characterized mainly by two nucleotide binding sites: N1 (upstream of the scissile phosphodiester bond) and N2 (downstream of it). These sites can be subdivided into subsites B1 and B2 (recognizing the base) and P1 and P2 (interacting with the phosphate). The cleavage specificity of most T2 RNases results from interactions at the B1 subsite (Deshpande and Shankar, 2002). In contrast, detailed biochemical characterizations of the substrate specificity of E^{rns} revealed that it cleaves preferentially NpU bonds (Hausmann et al., 2004); e.g., the

specificity is determined by interactions at the B2 subsite. Only the plant RNase MC1 isolated from bitter gourd (*Momordica charantia*) has a similar NpU cleavage specificity (Suzuki et al., 2000).

E^{rns} has nine conserved cysteine residues in the ectodomain, forming four conserved intrachain disulfide bonds (Langedijk et al., 2002). The C-terminal Cys171 residue makes an interchain disulfide that stabilizes an E^{rns} homodimer (Tews et al., 2009), as observed at the virion surface. While the interchain disulfide bridge is not essential for virus viability, as shown by the BVDV type strain NADL lacking Cys171, mutation of this cysteine in the context of an infectious cDNA clone of CSFV strain Alfort leads to attenuation in the animal host (Tews et al., 2009), suggesting a role of the covalent E^{rns} dimer in the viral cycle. Other RNases, like the bovine seminal RNase, a dimeric homolog of RNase A, are biologically active as homodimers, even though the monomeric molecule is also active (Lee and Raines, 2005).

The RNase activity of E^{rns} is not essential for virus viability in tissue culture (Hulst et al., 1998), but its abrogation also results in attenuation in the animal host (Meyer et al., 2002; Meyers et al., 1999). Although the mechanism for this attenuation is not understood at present, the ribonucleolytic activity of E^{rns} was reported to block activation of the innate immune system (Iqbal et al., 2004; Meyers et al., 1999). Soluble E^{rns} secreted from infected cells is found in the serum of infected animals at concentrations up to 50 ng/ml (Magkouras et al., 2008), and it was proposed to prevent induction of type I interferon (IFN) by enzymatic degradation of circulating dsRNA that otherwise would activate the IFN response via a Toll-like receptor (TLR)-dependent pathway (Magkouras et al., 2008; Mätzener et al., 2009). This is in line with the acid pH optimum of E^{rns} (pH 6.0) (Schneider et al., 1993; Windisch et al., 1996), which is consistent with cleavage of dsRNA in the endosome (Iqbal et al., 2004).

Here we report the crystal structure of the catalytic domain of E^{rns} from BVDV, including glycan chains attached to six N-glycosylation sites (NGS). We also describe the crystal structures of wild-type E^{rns} and a catalytic site mutant in complex with numerous mono- and oligonucleotide substrates that illustrate the structural basis of substrate binding. We provide a detailed analysis of the ribonucleolytic activity of E^{rns}, including the appearance and disappearance of poly(U) cleavage intermediates and accumulation of final cleavage products. Together with molecular docking and analyses of the kinetics of E^{rns} cleavage, this study provides a comprehensive picture of the catalytic mechanism of E^{rns}.

RESULTS AND DISCUSSION

Production and Crystallization of Catalytically Active E^{rns}

To produce recombinant E^{rns} from the BVDV-1 strain NCP-7, we used the *Drosophila* Expression System, which was used by others for the structure determination of viral glycoproteins (Kwong et al., 1998; Modis et al., 2003). A C terminally truncated version of the E^{rns} gene-spanning residues 1–207 (E^{rns}207; Figure 1; Table S1 available online) was inserted into a modified pMT/BiP-based expression plasmid containing a C-terminal double Strep-tag to allow for efficient affinity purification of E^{rns} from the S2 cell supernatant (Krey et al., 2010). This truncation was meant to avoid aggregation during secretion and/or crystallization of the protein caused by the predicted amphipathic helix at the C terminus that is not part of the structured ectodomain (Fetzer et al., 2005; Tews and Meyers, 2007).

Our production protocol resulted in yields of about 2–3 mg of glycoprotein per liter of supernatant fluid on average. Size exclusion chromatography analyses showed that approximately 70% of the glycoprotein eluted as monomer (~35 kD), whereas 30% eluted as dimer (~70 kD). We repeatedly observed spontaneous proteolysis of the purified protein around Leu165 after about 8–10 weeks at 4°C, yielding an N-terminal fragment (E^{rns}165).

To verify the catalytic activity of the recombinant protein species (E^{rns}165, E^{rns}207 monomer, and E^{rns}207 dimer), we determined the kinetic parameters k_{cat} and K_M of all three species using a synthetic 23-mer RNA oligonucleotide (see Experimental Procedures). We observed a 10-fold higher k_{cat} and K_M of monomeric E^{rns}207 and the E^{rns}165 fragment (Table S2), compared to a previous study performed with full-length dimeric E^{rns} (E^{rns}227) using a 57-nucleotide substrate of similar sequence (Hausmann et al., 2004). Differences in experimental conditions (e.g., substrate length, oligomerization state) as well as the C-terminal truncation may explain the kinetic differences between the two studies. The kinetic analysis using the dimeric species revealed an approximately fourfold (k_{cat} = 3.3) slower substrate cleavage compared to both monomeric species (k_{cat} = 11.9 and 11.5 for E^{rns}165 and E^{rns}207, respectively; the kinetic parameters are calculated per active site) and a higher substrate affinity, which is reflected in a slightly lower K_M (Table S2). This change could result from a perturbation of the active sites of the dimer, or it could be due to a two-step binding mechanism with the E^{rns}207 dimer having an increased affinity for the first binding step compared to the monomeric forms. This increased affinity to the dimer would then slow down the second binding step, resulting in an apparently decreased k_{cat} of the dimer.

While initial crystallization experiments with monomeric E^{rns}207 were unsuccessful, we obtained diffraction quality crystals from E^{rns}165, both by itself (Figure 1C) and in complex with several mono- and oligonucleotides (Figure 1D, E^{rns}+5′-UMP). The various crystals diffracted to a maximum resolution between 2.2 and 3.1 Å and belonged to various space groups (Tables 1 and S3). We determined the crystal structure of the apo-enzyme using experimental phases obtained by a single isomorphous replacement from a dysprosium derivative combined with anomalous diffraction from sulfur atoms in the native protein (see Experimental Procedures). The structures of the protein-substrate complexes were determined by the molecular replacement method using the native protein as search model.

Structure of BVDV E^{rns}165

The crystal structure reveals that the catalytic domain of E^{rns} adopts a slightly elongated shape with dimensions of about 47 × 31 × 31 Å, displaying a convex and a concave face (Figures 2A and 2C). It is folded as five α helices and seven β strands belonging to the α + β type structural class (Levitt and Chothia, 1976). The N and C termini of the polypeptide chain are approximately 18 Å apart. The model lacks approximately one quarter of

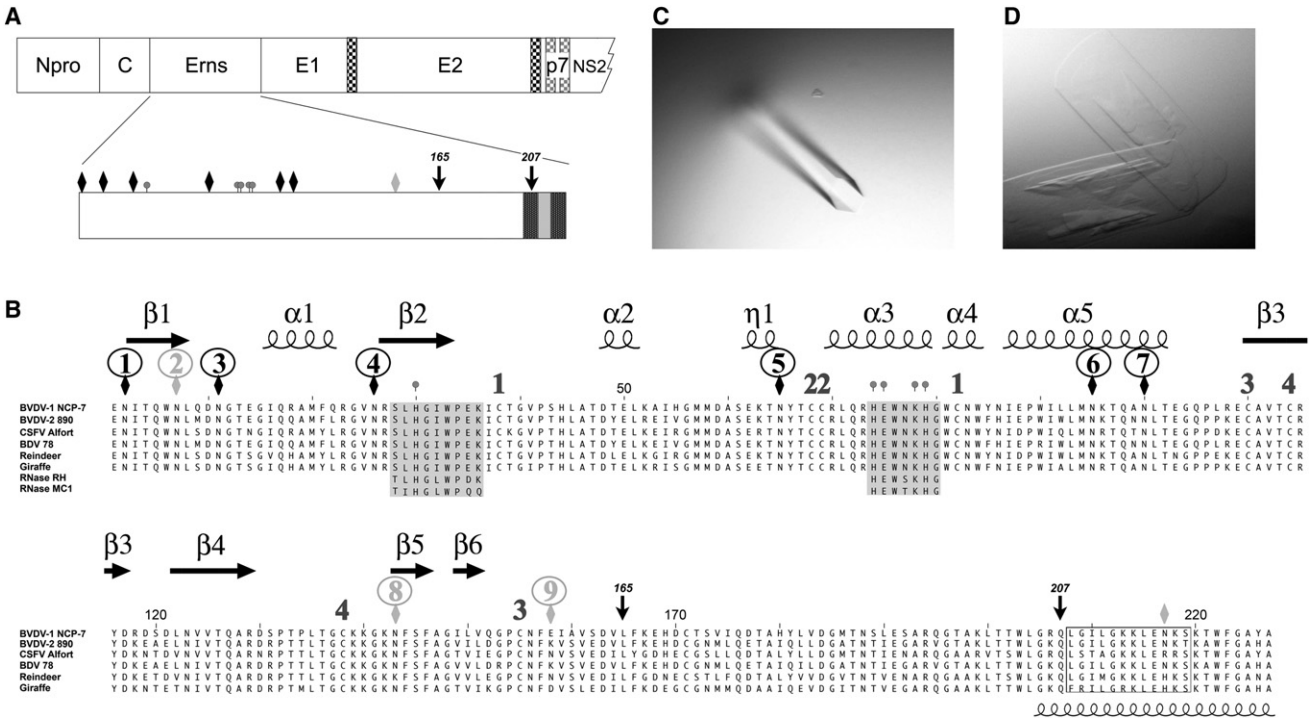

Figure 1. Primary Structure of BVDV NCP-7 E^rns

(A and B) Overview of the E^rns coding region (A) and alignment with E^rns of other pestiviruses and catalytic centers of two selected T2 RNases (B). Secondary structure elements taken from the crystal structure are shown above the sequence alignment. Catalytic residues are marked with gray circles. Black diamonds label N-glycosylation sites (NGSs) that are used in the NCP-7 strain of BVDV. Gray diamonds mark NGSs that are not used or present only in other pestiviruses. NGSs from all pestiviruses are numbered sequentially and the numbers shown within a circle. The eight cysteines, which form four intrachain disulfides, are numbered sequentially according to the disulfide bond. Amino acid stretches containing the catalytic residues are shaded, and a putative heparan binding site is boxed. Amino acids 165 and 207 are labeled by arrows. A spiral under the alignment indicates the reported C-terminal amphipathic helix.

(C and D) Crystals of E^rns165 grown in space group $P6_522$ (C) or complexed with 5′-UMP in space group $P2_12_12$ (D).

See also Table S1.

the molecule at its C-terminal side to complete the authentic E^rns. This missing region includes Cys171, which promotes homodimerization by forming an interchain disulfide bridge with its counterpart in an adjacent protomer. Unambiguous electron density was observed for residues 3–159, with the internal loop 106-110 displaying higher B factors and a poorer electron density than the rest of the polypeptide chain. The C-terminal residues 157–165 are juxtaposed to the loop 106-110, and in one crystal form (P6522), the C terminus is involved in crystal contacts on a twofold symmetry axis. This appears to induce a higher degree of disorder in that region, because in another crystal form (P21212), which has a different crystal packing, we observed clear electron density for both segments.

The structure of E^rns is stabilized by four intramolecular disulfide bridges (brown sticks, as shown in Figures 2A and 2C), confirming the previously reported disulfide connectivity (Langedijk, 2002). In BVDV strain NCP-7, E^rns contains seven potential NGS (Figures 1A and 1B). The fact that four of those are strictly conserved across all members of the genus *Pestivirus* indicates an important role of these carbohydrates in protein folding and/or function. We observed clear electron density for at least the first N-acetyl-glucosamine in six of seven potential sites (Figure 2A). For NGS1 and NGS3, where the glycans are stabilized by sugar-sugar contacts in the crystal, we observed carbohydrate chains of up to seven and five sugar residues, respectively (Figure 2B). To understand the protein surfaces that are compatible with glycosylation, we mapped the location of potential NGS appearing in the E^rns sequence across pestiviruses. This analysis revealed that the majority of them cluster on the convex side, with the exception of NGS2 present in CSFV and in the isolates Reindeer and Giraffe. The presence of glycans at the concave side appears to be selected against, likely because they would negatively impact on protein folding, oligomerization, or function. Homology modeling of CSFV E^rns using MODELLER (Sali and Blundell, 1993) showed that substitution of NGS2 would result in the glycan chain projecting within the concave side of the molecule and into the active site (Figures 2C and 2D; Table S1 lists the residues constituting the active site). Indeed, the side chains of the active site residues would be juxtaposed with the sugar chain, which would interfere with substrate binding. We therefore predict that this site is unlikely to be substituted in the corresponding strains. This prediction is strengthened by the fact that in the only two reported three-dimensional structures of N-glycosylated T2 RNases (which only have one carbohydrate chain each) (Ida et al., 2001; Matsuura et al., 2001), the glycans are also positioned at the convex side of the molecule. With respect to the structure of the homodimer, this clustering of N-linked glycans suggests that the concave surfaces form

Table 1. Crystallographic Data for E^{rns} and Selected E^{rns}/Nucleotide Complex Crystals, Data Collection, and Refinement

Variable	Erns165 native	E^{rns}165 + 5′-UMP	E^{rns}165H32K + CpUpC
Data collection			
Space group	P6522	P21212	P6522
Cell dimensions			
a, b, c (Å)	106.04, 106.04, 211.85	72.35, 107.97, 64.33	105.21, 105.21, 210.90
α, β, γ (°)	90, 90, 120	90, 90, 90	90, 90, 120
Resolution (Å)	50.00–2.20 (2.27–2.20)	48.07–2.23 (2.35–2.23)	41.82–3.01 (3.17–3.01)
R_{merge}	0.071 (0.497)	0.110 (0.471)	0.123 (0.516)
I/σI	14.4 (2.0)	12.4 (3.5)	10.7 (2.4)
Completeness (%)	97.2 (83.3)	100.0 (99.9)	95.6 (79.7)
Redundancy	4.9 (2.8)	6.1 (5.5)	3.6 (3.0)
Refinement			
Resolution (Å)	45.92–2.21	48.07–2.23	41.82–3.01
No. reflections	35,006	24,764	13,291
R_{work}/R_{free}	0.209/0.225	0.207/0.247	0.195/0.236
No. of atoms			
Protein	2,506	2,593	2,469
Ligand	–	85	57
Water	205	266	63
B factor			
Protein	42.29	28.63	47.86
rmsd			
Bond length (Å)	0.01	0.009	0.01
Bond angles (°)	1.26	1.1	1.20

Crystallographic data for the other complexes are given in Table S3. Values in parentheses correspond to the highest resolution shell. rmsd, root-mean-square deviation.
See also Table S3.

the interior of the dimer, like in a bivalve shell, while the heavily glycosylated convex surfaces form the exterior, with a glycan shield as protection from recognition by the immune system of the host.

The surface electrostatic potential of the E^{rns} catalytic domain reveals a rather negatively charged surface on the convex side (Figure 3A), while at the concave side it shows that the active site is mostly surrounded by positively charged patches (Figure 3B). The concave side thus displays a surface charge distribution that would be complementary to that of the negatively charged phosphate backbone of the substrate RNA. One patch of positively charged residues ($_{139}$KKGK$_{142}$) was reported previously to interact with dsRNA (Iqbal et al., 2004). The distribution of positive charges surrounding the active site and the absolute requirement for uridine for RNA cleavage (Hausmann et al., 2004) suggest a two-step interaction mode between E^{rns} and its substrate. While, in a first step, the positively charged concave surface and the RNA phosphate backbone would undergo nonspecific attractive electrostatic interactions, allowing for RNA scanning for scissile bonds, the strict base specificity of E^{rns} points to a second, highly specific interaction step involving the uridine base. Assuming that dimer formation results in a larger electrostatic surface in the interior of the dimeric molecule, and thus an increased affinity to the phosphate backbone of oligonucleotide substrates, such a two-step binding model would explain the differences in the kinetic parameters observed for monomeric and dimeric E^{rns} (Table S2).

Comparison with Other T2-RNases of Known Structure

A structural comparison of E^{rns}165 with the database using the DALI server revealed numerous T2 RNases as closest structural homologs (Table S4). The closest structural homolog is the plant T2 RNase MC1, which, as E^{rns}, has been shown to preferentially cleave NpU bonds (Irie et al., 1993).

We made a pairwise superposition of E^{rns} with MC1 (Figure 4A) and RNase Rh (*Rhizopus niveus*; data not shown), a plant RNase and a fungal RNase, respectively, representing the two main groups among T2 RNases. Plotting the distances between Cα atoms identified as structurally equivalent by the DALI-LITE server allowed a quantification of the structural similarity over the whole E^{rns} protein. This revealed that the secondary structure elements involved in the formation of the active site (β strands β1 and β2; α helices α3 and α5) are strongly conserved (Figures 4B and 4C). On the other hand, residues outside these secondary structure elements either are not classified as structurally equivalent or exhibit low structural similarity. These data therefore indicate that the requirement to maintain RNase activity has strictly dominated the divergent evolution of the molecules from a distant ancestor.

The structural alignment between E^{rns}165, RNase Rh, and MC1 also reveals that the two disulfide bridges common to plant, fungal, bacterial, and animal T2 RNases (Irie, 1999) are conserved in E^{rns} (disulfides 1 and 4; Figures 1 and 2), confirming their essential role for the folding of T2 RNases in general. In contrast, the two remaining disulfide bridges are structurally unrelated and have thus likely evolved only in the context of pestiviruses.

Substrate Binding and Base Specificity of E^{rns}

To better understand the NpU cleavage specificity of E^{rns} (Hausmann et al., 2004), we determined crystal structures of E^{rns} in complex with seven different mono-, di- and oligonucleotide substrates (or substrate analogs). We observed no differences in protein structure in the absence and presence of the various substrates, indicating that the enzyme undergoes no conformational changes upon nucleotide binding.

The N1 Site

The structures of the complexes revealed two conserved substrate binding sites (Figure 5C). Three different nucleotides (5′-CMP, 2′-UMP, and 5′-UMP) were found occupying the first site in the corresponding complex structures, bound through the phosphate moiety. This is illustrated by the crystal structure of the E^{rns}/5′-CMP complex (Figures 5D and 5E). In the apoenzyme structure, this region was occupied by a sulfate ion derived from the crystallization buffer, the presence of which was required for crystal formation. We observed that a nucleotide bound to this site only if its concentration exceeded that of sulfate in the crystallization conditions, suggesting direct competition. The nonselective nucleotide binding mode via the

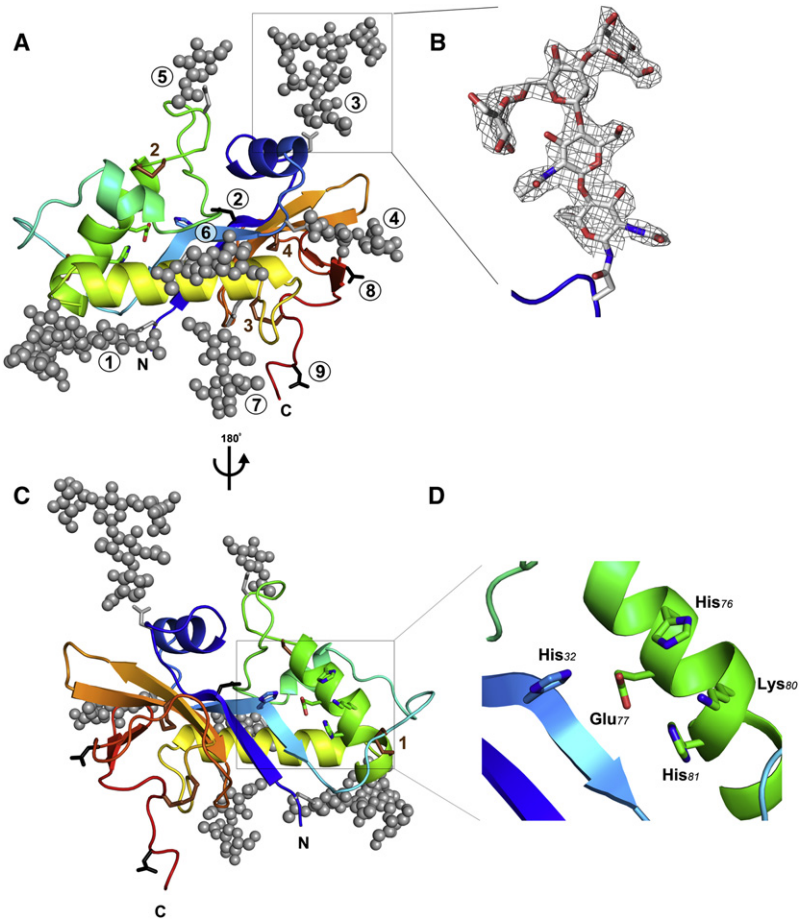

Figure 2. Three-Dimensional Structure of E^rns165

E^rns165 is colored as a ramp from blue to red through yellow, from N terminus to C terminus (labeled N and C, respectively). Disulfide bridges are depicted as brown sticks and numbered as in Figure 1 with brown numbers.

(A) View on the convex side of the molecule. Asparagine side chains of potential N-glycosylation sites are shown as gray (substituted) or black (present in other pestiviruses or not substituted) sticks, and the respective N-linked glycans are depicted as gray spheres and numbered as in Figure 1 within circles.

(B) Composite omit map, contoured at 1 sigma, around NGS3. The electron density for five sugar residues is very clear.

(C) View on the concave face of the molecule displaying the putative active site of the enzyme. The N-linked glycans cluster on the convex face of the molecule.

(D) Active site of BVDV E^rns including His32, His76, Glu77, Lys80, and His81.

phosphate moiety suggests that this site is part of the N1 site of T2 RNases—more precisely, the P1 subsite. The nucleotide phosphate makes hydrogen bonds with His76, Lys80, His81, and, potentially, to Trp35 (observed only for 5′- UMP; shown in dark gray in Figures 5D and 5E), showing that the P1 subsite is mainly formed by the catalytic residues of the enzyme. Table S5 lists all protein-substrate interactions from the crystal structures of 5′-UMP bound to E^rns and to MC1, respectively, the only three-dimensional structure of a NpU-specific T2 RNase available to date. All residues forming the P1 subsite are highly conserved among all T2 RNases (Irie, 1999). In the complexes with 5′-CMP, 5′-UMP, and 2′- UMP, the pyrimidine base makes stacking interactions with Trp35 (Figure 5D), which are stabilized by a hydrogen bond between an Arg131 Nη2 atom and the O2 atom of the 5′-CMP and 5′-UMP. Our data with 3′-AMP show the phosphate bound at the P1 subsite, but the base is disordered (data not shown). Although we did not obtain crystals of 3′-UMP bound to the enzyme, the similar position of the base in the three pyrimidine nucleotide complexes mentioned earlier suggests that the base would be found at the same place, given the torsional flexibility of the ribose moiety. We therefore interpret this site as a putative B1 subsite, which is not base-specific.

The N2 Site

The second nucleotide binding site (N2) is formed by a pocket lined by residues Asn9, Gln19, Gln129, His32, Ile18, Ala62, and Leu73 (Figures 5A and 5B, in red), which are less conserved among T2 RNases. This pocket was occupied exclusively by nucleotides containing a uracil ring, identifying the B2 subsite. Asn9 (Nδ2 and Oδ1 atoms) and Gln19 (Nε2) make three hydrogen bonds with the O4, N3, and O2 atoms of the base, respectively (Figures 5A and 5B). Uracil differs from cytosine—which did not bind to this pocket—only by an amino group replacing the O4 atom of uracil. This suggests that the observed hydrogen bond between O4 and Asn9 is crucial for the high-affinity binding of E^rns to uridine, and indirectly for the NpU cleavage specificity of E^rns. While the P1 subsites of E^rns and MC1 are clearly homologous, the residues constituting the uracil binding pockets in both E^rns and MC1 are different (Figures 6A and 6B). One possible interpretation could be that convergent evolution led to the independent formation of a uracil binding pocket in both enzymes. We cannot completely rule out, however, that an enzyme-specific evolutionary pressure led to divergent evolution of the uridine binding pocket from a common ancestor having NpU cleavage specificity.

5′-UMP Binding

Based on the cleavage specificity, the smallest ligand that would be able to bind at both N1 and N2 sites of E^rns simultaneously is 5′-UMP, for which the phosphate moiety would be expected to interact with the P1 subsite, while the uridine binds at the B2 subsite, as shown by the structure of the MC1/5′-UMP complex (crystallized in the absence of sulfate or phosphate ions, Protein data Bank [PDB] 1UCD). Unexpectedly, in the 5′-UMP complex, we did not observe the nucleotide binding simultaneously with the base at the uridine-specific B2 subsite and the phosphate at the P1 subsite. We found instead two separate nucleotides bound to the protein, one occupying the N1 site bound by the phosphate and the other occupying the N2 site, interacting via the uridine base. Moreover, we found that the uracil base at the B2 subsite was oriented such that the ribose points away

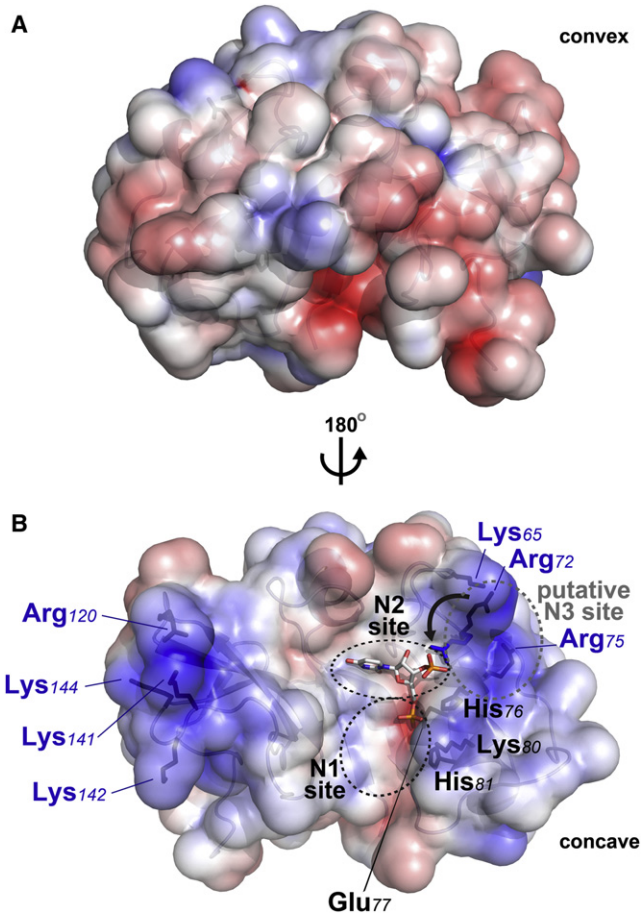

Figure 3. Electrostatic Surface Potential

(A and B) View of the convex face (A, oriented as in Figure 2A and lacking the glycans) and the concave face (B, oriented as in Figure 2C) of the molecule harboring the putative active site. The active site is surrounded by basic patches that represent positive charges likely contributing to the binding of negatively charged RNA substrates. Two positively charged patches ($_{120}$R/$_{141}$KKGK$_{144}$ and K$_{65}$R$_{72}$) are highlighted. The electrostatic potential, represented ramp-colored from red (negative) to blue (positive) through white (neutral), was calculated using APBS and contoured on a scale ranging from −4 to 4 kT/e. The two nucleotide binding sites, N1 and N2, are indicated by black dashed circles, and a putative N3 site is circled in gray. The molecular docking results obtained using pUp are displayed in sticks, as is Arg72, the side chain of which changes rotamer during molecular modeling to hydrogen bond the 3′ phosphate, forming a putative P2 subsite. A curved black arrow indicates the change in the side chain conformation when compared to the crystal structure.

from the P1 subsite, whereas in MC1 the ribose is directed toward the P1 subsite, as discussed later.

Why is simultaneous binding of 5′-UMP to both P1 and B2 subsites not observed in our E^{rns} crystals? A possible reason could be a kinetic effect: The B2 subsite displays high affinity for the uracil base (as discussed later), which would lead to binding of the base while the P1 subsite is still occupied by sulfate. This could induce binding of the nucleotide such that the base is trapped in the wrong orientation. Subsequent replacement of sulfate by 5′-UMP leads to the ternary complex observed in the crystal. However, given that the complexes were prepared beforehand, in the absence of sulfate, and then set to cocrystallization, we consider such a kinetic effect not likely. It is more likely that simultaneous binding is energetically less favorable than the observed binding of two separate mononucleotides, which does not reflect the physiological nucleotide ligands. The kinetic studies described next support this interpretation.

Kinetic Analysis of E^{rns} Cleavage Products

To further characterize the catalytic activity, we performed a kinetic analysis of poly(U) cleavage by E^{rns} using size exclusion chromatography (SEC). While E^{rns}165 wild-type (wt) cleaved poly(U) in a concentration-dependent manner, no cleavage was observed for poly(U) incubated with the active-site mutant E^{rns}165 H32K (Iqbal et al., 2004), demonstrating the specific catalytic activity of E^{rns}165 wt.

Poly(U) cleavage resulted in a broad distribution of fragment lengths, covering oligonucleotides from one to >100 nucleotides (Figure 7A, top panel), strongly suggesting a nonprocessive, random pattern of E^{rns} cleavage—at least for poly(U). The substrate was rapidly degraded, accumulating small fragments from one to six nucleotides (Figure 7A, bottom panel), which were eventually converted to mononucleotides. We characterized the cleavage of the accumulating smaller fragments by fitting the corresponding chromatograms with log-normal shapes and estimated their cleavage rate constants. The oligonucleotides sequentially disappeared (from the hexanucleotide to the dinucleotides; Figure S1), with long fragments being cleaved much faster than short ones (<6 nucleotides). This effect was not only due to the higher number of scissile bonds present in the longer oligonucleotides, as indicated by cleavage rate constants corrected for the number of scissile bonds (per-bond rates) of 0.04 and 0.025 s^{-1} for U6 and U5, respectively; 0.0068 and 0.005 s^{-1} for U4 and U3, respectively; and 0.0005 s^{-1} for U2 (Table S6). Even if these values are not very precise, they are consistent in all the experiments and indicate a large difference between the cleavage rate of U2 and that of longer fragments (U3–U6). This increase in per-bond cleavage rate with the length of the oligonucleotide, in particular between U2 and U3, was unexpected and strongly suggests the existence of a third nucleotide binding site in addition to N1 and N2.

Catalytic Mechanism

T2 RNases, like T1 RNases and RNase A, catalyze two distinct reactions. The first one (transphosphorylation) results in cleavage of the phosphodiester bond connecting two nucleotides bound at the N1 and N2 sites, respectively, and release of a 2′,3′-cyclophosphate nucleotide (5′-product) and a 5′-OH nucleotide (3′-product). The second catalytic function corresponds to the enzymatic hydrolysis of the 2′,3′-cyclophosphate nucleotide and release of a linear 3′-phosphate nucleotide (Figure 7C).

Analysis of 2′,3′-cUMP conversion to 3′-UMP by E^{rns} wt, but not by the catalytically inactive E^{rns}165 H32K (data not shown), demonstrated that E^{rns} catalyzes, in addition to the transphosphorylation reaction, also the hydrolysis step. Poly(U) cleavage by E^{rns} initially resulted in the release of 2′,3′-cyclophosphate oligo- and mononucleotides with no 3′-UMP release, as shown by ^{31}P-NMR (Figures 7B and 7C, second and third panels). This indicates that the two distinct catalytic functions of E^{rns}

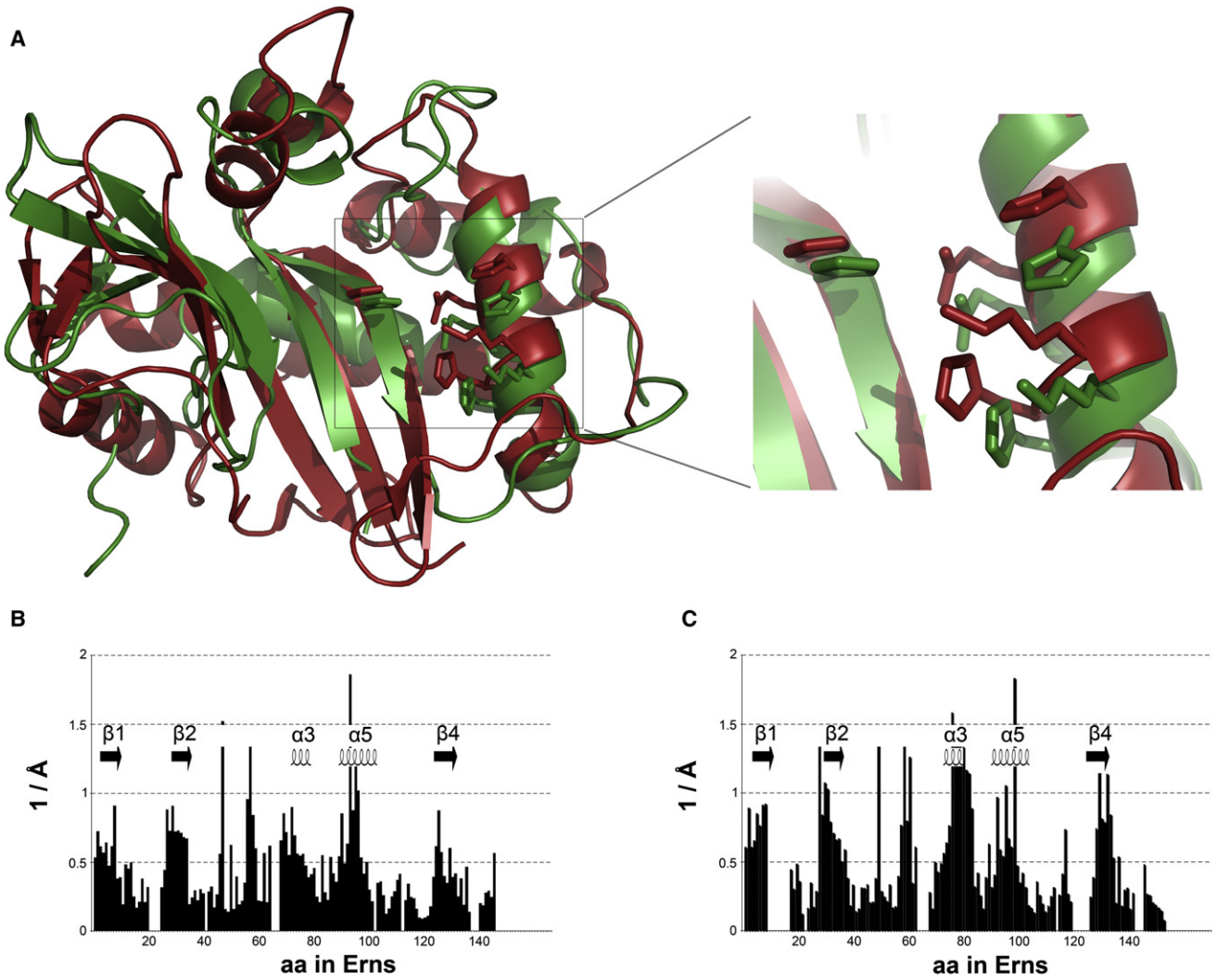

Figure 4. Structural Homology to Other T2 RNases

(A) E^{rns}165 (green) superposed to MC1 (red, a plant T2 RNase) using the DALI-LITE server (Holm and Park, 2000). A close-up view on the active site (right panel) shows the side chains of the five catalytic residues.

(B and C) Plot of the distances (as reciprocal values to highlight the closest segments by high values) between the structurally equivalent Cα-atoms (as assigned by the DALI-LITE server) for E^{rns}-MC1 (B) and E^{rns}-RNase Rh (C). Gaps indicate Cα-atoms in E^{rns} that were found not to have a structural equivalent. Secondary structure elements composing the active site are shown as arrows and spirals, respectively.

See also Table S4.

are uncoupled and the 2′,3′-cyclophosphate nucleotide dissociates from the enzyme prior to de novo binding to undergo enzymatic hydrolysis of the cyclophosphate moiety. A large increase (~1,700×) of enzyme concentration was required to partially convert 2′,3′-cUMP to 3′-UMP after 1,000 min (Figures 7B and 7C, bottom panels). We crystallized the enzymatically active enzyme in complex with 2′,3′-cUMP and observed the nucleotide bound at the B2 subsite, as expected, and the distance of the cyclophosphate to the P1 subsite was 10 Å (Figure S3). This distance is incompatible with enzymatic hydrolysis of 2′,3′-cUMP bound at the B2 subsite, indicating that dissociation from the B2 subsite and de novo binding to the P1 subsite is required for hydrolysis. This, together with the low efficiency of the reaction as monitored by the kinetic analysis, suggests a competition between P1 and B2 subsites for nucleotide binding in favor of the B2 subsite. In conclusion, the protracted hydrolysis indicates that the B2 subsite not only confers the substrate specificity to the enzyme, but it also has a higher affinity and thus constitutes the primary substrate recognition site of E^{rns}.

The active site of BVDV E^{rns} has been determined to consist of His32, His76, Glu77, Lys80, and His81 (Hulst and Moormann, 2001) (Figure 2D), in agreement with single-site mutations rendering the enzyme catalytically inactive (Hulst et al., 1998; Meyers et al., 1999). Superposition of the catalytic residues of E^{rns} and MC1 demonstrates their structural homology (Figure 4A)—as previously reported for plant and fungal T2 RNases (Tanaka et al., 2000)—and indicating similar cleavage

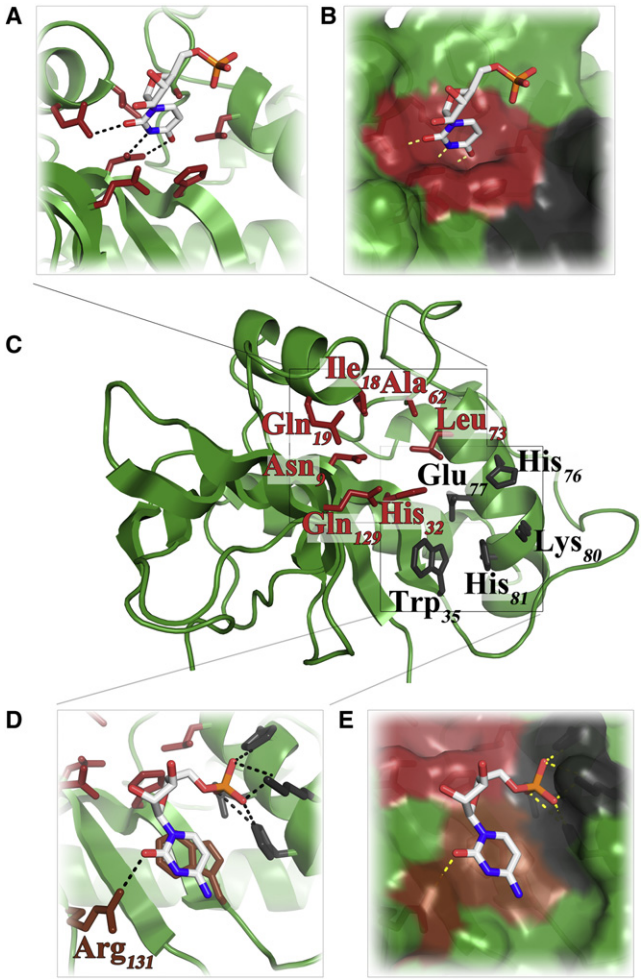

Figure 5. Nucleotide Binding Mode

The two major nucleotide binding sites observed in E^rns are depicted with their corresponding side chains in red (B2 subsite) and dark gray (P1 subsite). Nucleotide ligands and side chains forming the two subsites are displayed as sticks. Dotted lines represent hydrogen bonds.

(A and B) The B2 subsite binds exclusively uracyl nucleotides via hydrogen bonding between the base and residues Asn9 and Gln19, here shown for 5′-UMP.

(C) The disposition of the two sites on E^rns165.

(D and E) The P1 subsite binds nucleotides via their phosphate moiety by hydrogen bonding to His76, Lys80, and His81. The base of the corresponding nucleotide binds at the B1 subsite (brown), making a stacking interaction with Trp35 as observed for 5′-CMP (shown here) and 5′-UMP (data not shown), supported by a hydrogen bond from the O2 atom of the base to Arg131 Nη2. See also Table S5 and Figures S3 and S4.

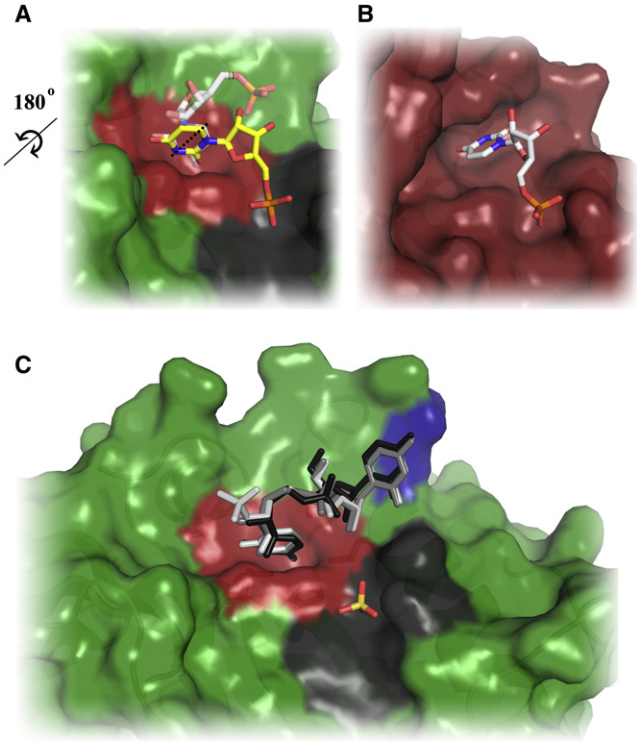

Figure 6. Simultaneous Substrate Binding to P1 and B2 Subsite of E^rns and MC1

(A) 5′-UMP obtained by molecular docking to E^rns, colored in yellow, bound to both P1 and B2 subsites simultaneously. The uridine in the B2 subsite was rotated by 180° around an axis through N3 and C6 atoms of the uracil (indicated by a dotted line) when compared to the crystal structure (shown in transparent gray sticks, see Figure 5b). E^rns is shown in surface representation and colored as in Figure 5.

(B) 5′-UMP bound to both P1 and B2 subsites of MC-1 in the crystal structure (PDB 1UCD).

(C) E^rns in complex with oligonucleotide substrates. The protein is shown in surface representation and the ligands—a trinucleotide CpUpC (light gray), a dinucleotide CpU (gray), and a nonhydrolysable dinucleotide CpsU (dark gray)—are displayed as sticks. The sulfate ion bound to the P1 subsite is also shown in sticks. Positively charged Arg72, which likely serves as additional binding site, is colored blue.

See also Figure S2.

mechanisms. The catalytic mechanism proposed previously for RNase Rh (Irie, 1997), together with the structural details revealed in this study, indicate that the transphosphorylation reaction proceeds as follows: His81 of E^rns acts as a catalytic base, initiating the reaction by withdrawal of a hydrogen atom from the 2′-OH group of the ribose with a nonprotonated Nε2 atom. This results in the nucleophilic O2 atom of the ribose attacking the phosphorus atom. The intermediate pentacoordinated phosphate is stabilized by protonated His76, Glu77, and Lys80; protonated His32 acts as hydrogen donor to release the cleavage products.

Divalent cations, and Zn^{2+} ions in particular, have been reported to inhibit the catalytic activity of E^rns (Schneider et al., 1993; Windisch et al., 1996). We therefore also determined the structure of BVDV E^rns in the presence of Zn^{2+}, which showed a Zn^{2+} ion bound to His81 (data not shown), thus highlighting the role of this residue as catalytic base. A pKa calculation based on the E^rns coordinates using PROPKA 3.0 (Rostkowski et al., 2011) revealed pKas of 10.42 for Lys80, 7.18 for Glu77, 5.46 for His76, 5.28 for His32, and 4.31 for His81. E^rns was reported previously to cleave in a wide pH range between 4.5 and 7.3 (Windisch et al., 1996). This pH profile is in agreement with the pKa values of the active site residues, in particular of Glu77 and His81, illustrating the requirement of an unprotonated imidazole nitrogen atom in the catalytic base (His81) to attack

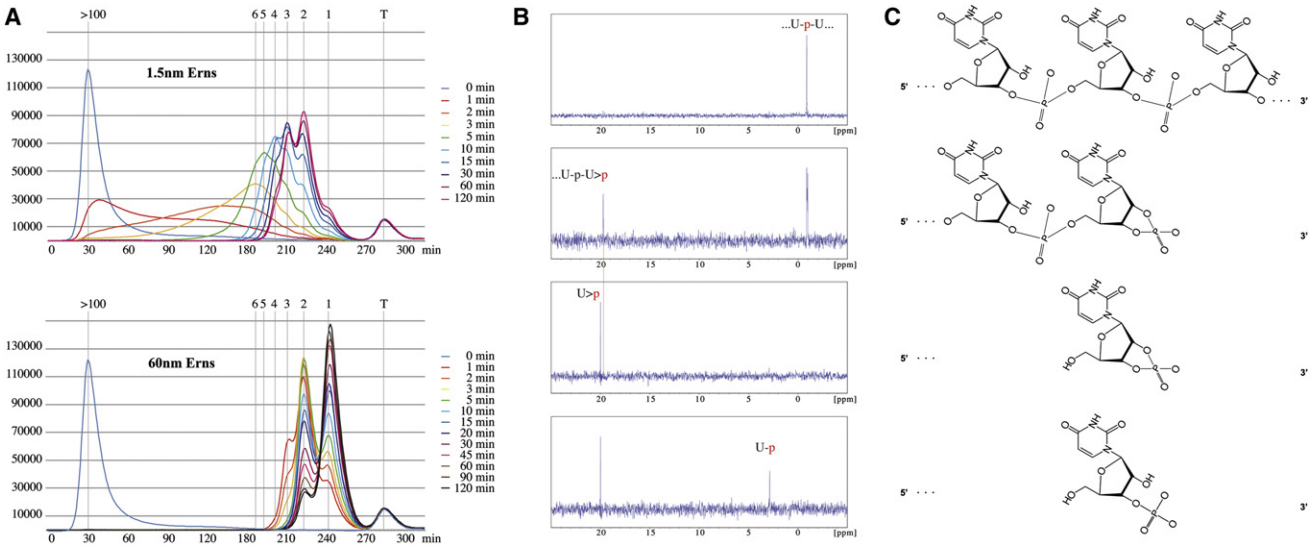

Figure 7. Biophysical Analysis of E^rns Cleavage Products

Analysis of poly(U) fragments resulting from E^rns cleavage by SEC, in (A), and ^{31}P nuclear magnetic resonance (NMR), in (B).

(A) One millimole of poly(U) was incubated with E^rns for different times and then subjected to SEC analysis monitored by absorbance at 270 nm; the absorption curves corresponding to the various cleavage times are colored according to the key. Twelve micromoles of thymine was added to the sample prior to the analysis to allow for chromatogram calibration.

(B) E^rns cleavage of poly(U) monitored by ^{31}P NMR. One-dimensional ^{1}H-decoupled ^{31}P spectra were recorded every 20 min during 10 hr. Specific peaks were observed corresponding to poly(U) linear phosphate (top panel; time 0) at 19.7 ppm for cyclophosphate oligonucleotides (second panel, represented by ..U-p-U>p), at 20 ppm for cyclophosphate mononucleotide (third panel), and at 2.9 ppm for 3′ linear phosphate mononucleotide (bottom panel).

(C) Illustration of the sequentially emerging cleavage products of poly(U) cleavage by E^rns in each of the corresponding panels in (B).

See also Figure S1.

the 2′-OH group and a protonated Glu77 to polarize the p = O bond or to stabilize a pentacovalent intermediate.

Binding of Oligonucleotides to E^rns

As discussed earlier, binding of mononucleotides does not reflect the physiological RNA binding, and our kinetic analysis suggested that cocrystallization with di- and trinucleotides would be more informative. However, the maximum oligonucleotide concentrations obtained for such experiments were too low to displace the sulfate ion necessary for crystallization, and none of the structures we obtained—E^rns in complex with CpU, CpsU, and CpUpC—had a nucleotide phosphate bound at the P1 subsite, which was occupied by sulfate in each case. We confirmed the relevance of the sulfate competition by measuring a sulfate concentration-dependent inhibition of the catalytic activity of E^rns (Figure S2). Extensive crystallization trials at lower sulfate concentrations—<120 mM $(NH_4)_2SO_4$—in an attempt to trap a physiologically relevant substrate binding mode were unfortunately unsuccessful.

To confirm that simultaneous binding of a nucleotide substrate at both P1 and B2 subsites of E^rns is possible, we performed a molecular docking analysis with E^rns and 5′-UMP using AutoDock Vina (Trott and Olson, 2010). In parallel, experiments with MC1 and 5′-UMP were carried out to verify the reliability of the docking experiment. This control showed that the 5′-UMP/MC1 complex obtained by docking matched very well the complex observed by X-ray crystallography, spanning both P1 and B2 subsites (Figure 6B). Molecular docking of 5′-UMP to the E^rns structure revealed a similar 5′-UMP orientation, binding to both P1 and B2 subsites (Figure 6A). The uracil ring docked to the B2 subsite was rotated by 180° around an axis through the N3 and C6 atoms of the base (indicated with a dotted line in Figure 6A), compared to the 5′-UMP orientation in the crystal structure of the complex (indicated with transparent gray sticks in Figure 6A).

In the crystal structures of E^rns complexed with di- or trinucleotides we found the uracil base bound at the B2 subsite and a cytosine base juxtaposed to the positively charged patch around Arg72 (Figures 3B and 6C, colored in blue), suggesting a putative binding site (N3) for the base downstream of the uridine. The RNA backbone was oriented in each case in the 3′→5′ direction between the B2 subsite and the putative N3 site and not, as expected, in the 5′→3′ direction. The presence of a sulfate ion at the P1 subsite thus imposes that the uracil base again binds in the same orientation as in the case of the mononucleotides (Figure 6C), which projects the ribose ring away from the protein (Figure 6A). The increased distance from the ribose to the putative N3 site can only be bridged by the longer C4*-C5*-O5*-P bonds, connecting to the 5′ phosphate and spanning approximately 3.9 Å, but not by the shorter C3*-O3*-P bonds, which span only 2.7 Å (Figure S4). The presence of sulfate therefore indirectly imposes that the oligonucleotide chain binds in the opposite direction, which is feasible because of the flexibility of the RNA backbone. Molecular docking using a 5′,3′-uridine diphosphate (pUp) as a ligand and a flexible Arg72 side chain revealed a substrate orientation similar to the one obtained for 5′-UMP, with the 3′ phosphate forming two hydrogen bonds to the Arg72 Nη1 and Nη2 atoms (displayed

in Figure 3B). This strongly suggests that the positively charged patch around Arg72 (Figure 3B) serves as additional binding site for the downstream phosphate of the uridine and potentially also for the downstream base (P2 subsite and putative B3 subsite).

Conclusions

Taken together, our results make clear that binding and cleavage of an RNA polynucleotide substrate to yield linear nucleotide 3′-monophosphates by E^{rns} is a multistep process. Initially, rapid substrate degradation results in the accumulation of small 2′,3′-cyclophosphate oligonucleotides. These are degraded to 2′,3′-cyclophosphate mononucleotides, with considerably varying rate constants for different fragment species, the main limiting step being the cleavage of dinucleotides. Eventually, hydrolysis of the 2′,3′ cyclophosphates occurs as a slow reaction, releasing the linear nucleotide 3′-monophosphates as final cleavage product. The use of the nonphysiological poly(U) as substrate has thus enabled us to make a careful dissection of the catalytic mechanism of E^{rns}. In combination with the structural data, these results provide a comprehensive picture of the substrate binding and catalytic mechanism of E^{rns}. Despite the nonphysiological binding of mononucleotides and oligonucleotides in the presence of sulfate, the availability of a structure of a homologous T2 RNase with the same specificity in complex with 5′-UMP allows us to interpret the data, by resorting to molecular docking, to provide the functional model illustrated in Figure 3B. Further studies are required, however, to define the precise role of the RNase activity during the viral cycle and understand the interplay between virus and the innate immune system of the host (Iqbal et al., 2004; Magkouras et al., 2008; Meyers et al., 1999).

On a different register, the crystal structure of E^{rns} clearly demonstrates that pestiviruses acquired a RNase gene from the T2 RNase family, highlighting the important genetic exchanges that have taken place between viruses and cells during evolution. For several T2 RNases, catalytic-independent roles were reported recently (Luhtala and Parker, 2010), and pestivirus E^{rns} was also described to have catalytic-independent roles in the virus cycle (Tews et al., 2009; Widjojoatmodjo et al., 2000). However, retention of structural similarity at the catalytic site with plant T2 RNases highlights the evolutionary advantage for pestiviruses to maintain an enzymatically active RNase. In addition, the observation that mutation of the E^{rns} catalytic center results in attenuation of the virus in its natural host underlines the importance of the RNase activity in the virus cycle, in particular considering the viral "infect and persist" survival strategy (Peterhans and Schweizer, 2010).

EXPERIMENTAL PROCEDURES

Expression Constructs, Production, and Purification of E^{rns}

Truncated versions of BVDV E^{rns} wt and the inactive mutant E^{rns}H32K (Iqbal et al., 2004) (residues 1-207) were cloned into a modified *Drosophila* S2 expression vector described previously (Krey et al., 2010). The C-terminal 20 residues of E^{rns} were excluded to avoid potential problems during secretion, purification and/or crystallization due to a putative C-terminal amphipathic helix (Tews and Meyers, 2007). *Drosophila* S2 cells were transfected as described (Johansson et al., 2012). For large-scale production, cells were induced with 500 μM $CuSO_4$ at a density of approximately 7 × 10^6 cells per milliliter for 8 days and pelleted, and E^{rns}207 was purified by affinity chromatography from the supernatant using a StrepTactin Superflow column followed by SEC using a Superdex75 column. Pure monomer was concentrated to approximately 5 mg/ml. After storage of concentrated monomeric protein for ~10 weeks at 4°C, further processing of unknown origin reproducibly removed the C-terminal 82 residues including the Strep-tag (E^{rns}165).

Crystallization, Data Collection, Structure Determination, and Refinement

Crystals of E^{rns}165 were grown at 293 K using the hanging-drop vapor diffusion method in drops containing 1 μl protein or complex solution (3–5 mg/ml in 10 mM TRIS, pH 8.0, 150 mM NaCl, complexed with 10–110 mM of the respective nucleotide substrate) mixed with 1 μl reservoir solution containing 32%–34% (w/v) polyethylene glycol (PEG) 2000 monomethylether, 120–170 mM $(NH_4)_2SO_4$, 80 mM KH_2PO_4, and 100 mM sodium acetate (pH 4.6). Diffraction quality rod-like (native protein, Zn^{2+}, CpsU, CpU, and CpUpC) or plate (2′-UMP, 5′-UMP, 5′-CMP, and 2′-3′-cUMP) crystals appeared after 1 week and were flash-frozen in mother liquor containing 15%–25% (v/v) PEG 400. Spacegroups and cell dimensions of the crystals, resolution limits, data collection details, and refinement statistics are summarized in Tables 1 and S3.

Data were collected at the Swiss Light Source (PX I), the European Synchrotron Radiation Facility (beam lines ID23-1, ID14-4, and ID23-2) and the Synchrotron Soleil (Proxima 1). Data were processed with XDS (Kabsch, 1988), and scaling and reduction was performed using Pointless (Evans, 2006) and programs from the CCP4 suite (CCP4, 1994). Initial experimental phases were obtained from a crystal soaked for 30 min in a 20 mM dysprosium chloride ($DysCl_3$) solution in cryo buffer. Data were collected at a wavelength corresponding to the LI edge of dysprosium (1.1765 Å) on a single crystal using inverse beam data collection strategy with wedges of 10°. The experimental phases were obtained by the single isomorphous replacement method and refined using the anomalous signal of a highly redundant sulfur-SAD data set collected at 1.6951 Å on crystals of the native protein. Experimental phasing was performed using AutoSharp (Vonrhein et al., 2007), and the crystal structures of the enzyme-substrate complexes were determined by the molecular replacement method using Phaser (McCoy et al., 2007) and the structure of the apoenzyme as a model. Model building was performed using Coot (Emsley et al., 2010), and refinement was performed using AutoBuster (Bricogne et al., 2010).

Determination of Enzyme Activity

We labeled 100 picomol of oligonucleotide 23AU (5′-AAAAAAAAAAAAAUAAAAAAAA) with 0.925 MBq of [γ-^{32}P] adenosine-triphosphate using 10 U of T4 polynucleotide kinase for 45 min at 37°C. The enzyme was heat-denatured, and the mix was diluted to 100 μl in 40 mM Tris, pH 6.4, 5 mM EDTA. Routinely more than 95% of the radioactivity was transfered to the oligonucleotide as assessed by polyacrylamide gel electrophoresis, eliminating the need for further purification.

Ten, 20, 40, and 80 picomol of unlabeled 23AU were spiked with 1 picomol (9.25MBq) of ^{32}P-23AU in 40 mM Tris acetate and 0.5 mM EDTA, pH 6.0, giving final concentrations of 0.5, 1, 2, and 4 μM. A total of 0.2 pmol of either E^{rns} protein (E^{rns}165, E^{rns}207-monomer, and E^{rns}207-dimer) was added for 0, 5, 15, and 30 s at 37°C, and reactions were stopped by rapid mixing with 95% formamide followed by snap freezing in liquid N_2. After heating for 3 min at 72°C samples were separated by SDS-PAGE using gels with 8.3 M urea, which were subsequently analyzed by phosphoimaging. All experiments were performed at least in triplicate.

The kinetic parameters K_M and Vmax of 23AU for the three enzymes E^{rns}165, E^{rns}207-dimer, and E^{rns}207-monomer were determined essentially as described elsewhere (Fersht, 1977; Hausmann et al., 2004).

Gel-Filtration Kinetic Analysis

To determine kinetics of poly(U) cleavage by E^{rns}165 using SEC, 1 millimol of poly(U) (expressed in terms of mononucleotide) was incubated in the presence of 1.5, 15, and 60 nM enzyme in 100 μl of 10 mM Tris acetate buffer at pH 5.8 at 25°C. Aliquots of 5 μl were taken at 1, 2, 3, 5, 10, and 15 min and at various times between 20 and 120 min, quenched in 20 μl of 50 mM phosphate, pH 7.0, 200 mM NaCl, 15 μM thymine and stored on ice until the SEC (Eprogen CG101-25, 250 × 4.5 mm, filled with GPC-100 glycerol-bonded 5 μ/100 Å spherical silica, flow rate, 0.4 ml/min). Control samples containing E^{rns}H32K

were prepared identically, incubated at 25°C throughout the experiment, and analyzed after all time points.

The chromatograms were normalized using the thymine peak and those corresponding to the elution of small species (from mono- to hexanucleotides) were manually fitted by using log-normal shapes. The rate constants for fragments U_4, U_3, U_2, and U_1 were approximated using Copasi[42] and the oligonucleotide amounts were determined by the chromatogram fitting at early time points (60 nm E^{rns}) considering the following first-order processes with the corresponding independent rate constants: $U_4 \rightarrow U_3 + U_1$ (with k_{43} rate constant), $U_4 \rightarrow 2\times U_2$ (k_{42}), $U_3 \rightarrow U_2 + U_1$ (k_{32}), and $U_2 \rightarrow 2\times U_1$ (k_{21}).

NMR Analysis

Poly(U) cleavage by E^{rns} was followed by ^{31}P-NMR. Five hundred microliters of a 1 mM poly(U) solution in Tris acetate buffer (pH 6.3) was mixed with 3 nM or 5 μM E^{rns} wt or E^{rns}H32K. One-dimensional ^{1}H-decoupled ^{31}P-spectra were recorded every 20 min during 10 hr (offset: 10 ppm, spectral width: 30 ppm, time domain: 4k, 512 scans) in a 500 MH Avance II spectrometer (operating at the ^{31}P frequency of 202.456335 MHz) equipped with a direct broadband probe.

Molecular Docking

Crystal structures of MC1 (PDB 1UCD) and E^{rns} in complex with 5′-UMP were used for molecular docking experiments using Autodock Vina (Trott and Olson, 2010). Active site residues of both proteins were superimposed, and 5′-UMP was removed from the coordinate files. Subsequently, automatic docking of 5′-UMP to both protein molecules was performed in a search space of 15 × 20 × 18 Å centered on His32 of E^{rns}.

ACCESSION NUMBERS

Coordinates and structure factors of a total of nine crystal structures have been deposited in the Protein Data Bank under the accession numbers 4DVK, 4DVL, 4DVN, 4DW3, 4DW4, 4DW5, 4DW7, 4DWA, and 4DWC.

SUPPLEMENTAL INFORMATION

Supplemental Information includes four figures, six tables, and Supplemental Experimental Procedures and can be found with this article online at doi:10.1016/j.str.2012.03.018.

ACKNOWLEDGMENTS

T. K. benefited from an Institut Pasteur "Bourse Roux" and then from an EU Marie Curie fellowship (MEIF-CT-2007-04725). This work was supported by the ANR Grant ANR 05 MIIM 012 01 to F.A.R., in addition to recurrent funding by Institut Pasteur, CNRS, and Merck-Serono to F.A.R. We thank Gary L. Gilliland for helpful discussions, Ahmed Haouz and Patrick Weber from the crystallization platform for help in crystallization, and staff scientists from the synchrotron beam lines for help during data collection.

Received: January 30, 2012
Revised: February 29, 2012
Accepted: March 3, 2012
Published: May 8, 2012

REFERENCES

Bricogne, G., Blanc, E., Brandl, M., Flensburg, C., Keller, P., Paciorek, P., Roversi, P., Sharff, A., Smart, O., Vonrhein, C., and Womack, T. (2010). BUSTER version 2.9 (Cambridge, UK: Global Phasing Ltd.).

CCP4 (Collaborative Computational Project, Number 4). (1994). The CCP4 suite: programs for protein crystallography. Acta Crystallogr. D Biol. Crystallogr. *50*, 760–763.

Deshpande, R.A., and Shankar, V. (2002). Ribonucleases from T2 family. Crit. Rev. Microbiol. *28*, 79–122.

Durantel, D., Branza-Nichita, N., Carrouée-Durantel, S., Butters, T.D., Dwek, R.A., and Zitzmann, N. (2001). Study of the mechanism of antiviral action of iminosugar derivatives against bovine viral diarrhea virus. J. Virol. *75*, 8987–8998.

Emsley, P., Lohkamp, B., Scott, W.G., and Cowtan, K. (2010). Features and development of Coot. Acta Crystallogr. D Biol. Crystallogr. *66*, 486–501.

Evans, P. (2006). Scaling and assessment of data quality. Acta Crystallogr. D Biol. Crystallogr. *62*, 72–82.

Fersht, A.R. (1977). Enzyme structure and mechanism (New York: W.H. Freeman).

Fetzer, C., Tews, B.A., and Meyers, G. (2005). The carboxy-terminal sequence of the pestivirus glycoprotein E(rns) represents an unusual type of membrane anchor. J. Virol. *79*, 11901–11913.

Hausmann, Y., Roman-Sosa, G., Thiel, H.J., and Rümenapf, T. (2004). Classical swine fever virus glycoprotein E rns is an endoribonuclease with an unusual base specificity. J. Virol. *78*, 5507–5512.

Holm, L., and Park, J. (2000). DaliLite workbench for protein structure comparison. Bioinformatics *16*, 566–567.

Hulst, M.M., and Moormann, R.J. (2001). Erns protein of pestiviruses. Methods Enzymol. *342*, 431–440.

Hulst, M.M., van Gennip, H.G., Vlot, A.C., Schooten, E., de Smit, A.J., and Moormann, R.J. (2001). Interaction of classical swine fever virus with membrane-associated heparan sulfate: role for virus replication in vivo and virulence. J. Virol. *75*, 9585–9595.

Hulst, M.M., Panoto, F.E., Hoekman, A., van Gennip, H.G., and Moormann, R.J. (1998). Inactivation of the RNase activity of glycoprotein E(rns) of classical swine fever virus results in a cytopathogenic virus. J. Virol. *72*, 151–157.

Ida, K., Norioka, S., Yamamoto, M., Kumasaka, T., Yamashita, E., Newbigin, E., Clarke, A.E., Sakiyama, F., and Sato, M. (2001). The 1.55 A resolution structure of Nicotiana alata S(F11)-RNase associated with gametophytic self-incompatibility. J. Mol. Biol. *314*, 103–112.

Iqbal, M., and McCauley, J.W. (2002). Identification of the glycosaminoglycan-binding site on the glycoprotein E(rns) of bovine viral diarrhoea virus by site-directed mutagenesis. J. Gen. Virol. *83*, 2153–2159.

Iqbal, M., Flick-Smith, H., and McCauley, J.W. (2000). Interactions of bovine viral diarrhoea virus glycoprotein E(rns) with cell surface glycosaminoglycans. J. Gen. Virol. *81*, 451–459.

Iqbal, M., Poole, E., Goodbourn, S., and McCauley, J.W. (2004). Role for bovine viral diarrhea virus Erns glycoprotein in the control of activation of beta interferon by double-stranded RNA. J. Virol. *78*, 136–145.

Irie, M. (1997). [Structures and functions of ribonucleases]. Yakugaku Zasshi *117*, 561–582.

Irie, M. (1999). Structure-function relationships of acid ribonucleases: lysosomal, vacuolar, and periplasmic enzymes. Pharmacol. Ther. *81*, 77–89.

Irie, M., Watanabe, H., Ohgi, K., Minami, Y., Yamada, H., and Funatsu, G. (1993). Base specificity of two plant seed ribonucleases from Momoridica charantia and Luffa cylindrica. Biosci. Biotechnol. Biochem. *57*, 497–498.

Johansson, D.X., Krey, T., and Andersson, O. (2012). Production of recombinant antibodies in Drosophila melanogaster S2 cells. In Antibody engineering, P. Chames, ed. (Totowa, NJ: Humana Press), in press.

Kabsch, W. (1988). Automatic indexing of rotation diffraction patterns. J. Appl. Crystallogr. *21*, 67–72.

Krey, T., d'Alayer, J., Kikuti, C.M., Saulnier, A., Damier-Piolle, L., Petitpas, I., Johansson, D.X., Tawar, R.G., Baron, B., Robert, B., et al. (2010). The disulfide bonds in glycoprotein E2 of hepatitis C virus reveal the tertiary organization of the molecule. PLoS Pathog. *6*, e1000762.

Kwong, P.D., Wyatt, R., Robinson, J., Sweet, R.W., Sodroski, J., and Hendrickson, W.A. (1998). Structure of an HIV gp120 envelope glycoprotein in complex with the CD4 receptor and a neutralizing human antibody. Nature *393*, 648–659.

Langedijk, J.P. (2002). Translocation activity of C-terminal domain of pestivirus Erns and ribotoxin L3 loop. J. Biol. Chem. *277*, 5308–5314.

Langedijk, J.P., van Veelen, P.A., Schaaper, W.M., de Ru, A.H., Meloen, R.H., and Hulst, M.M. (2002). A structural model of pestivirus E(rns) based on

disulfide bond connectivity and homology modeling reveals an extremely rare vicinal disulfide. J. Virol. *76*, 10383–10392.

Lazar, C., Zitzmann, N., Dwek, R.A., and Branza-Nichita, N. (2003). The pestivirus E(rns) glycoprotein interacts with E2 in both infected cells and mature virions. Virology *314*, 696–705.

Lee, J.E., and Raines, R.T. (2005). Cytotoxicity of bovine seminal ribonuclease: monomer versus dimer. Biochemistry *44*, 15760–15767.

Levitt, M., and Chothia, C. (1976). Structural patterns in globular proteins. Nature *261*, 552–558.

Lindenbach, B.D., Thiel, H.J., and Rice, C.M. (2007). Flaviviridae: The viruses and their replication. In Fields Virology, Fifth Edition, D.M. Knipe and P.M. Howley, eds. (Philadelphia: Lippincott, Williams & Wilkins), pp. 1101–1152.

Luhtala, N., and Parker, R. (2010). T2 Family ribonucleases: ancient enzymes with diverse roles. Trends Biochem. Sci. *35*, 253–259.

Magkouras, I., Mätzener, P., Rümenapf, T., Peterhans, E., and Schweizer, M. (2008). RNase-dependent inhibition of extracellular, but not intracellular, dsRNA-induced interferon synthesis by Erns of pestiviruses. J. Gen. Virol. *89*, 2501–2506.

Matsuura, T., Sakai, H., Unno, M., Ida, K., Sato, M., Sakiyama, F., and Norioka, S. (2001). Crystal structure at 1.5-A resolution of Pyrus pyrifolia pistil ribonuclease responsible for gametophytic self-incompatibility. J. Biol. Chem. *276*, 45261–45269.

Mätzener, P., Magkouras, I., Rümenapf, T., Peterhans, E., and Schweizer, M. (2009). The viral RNase E(rns) prevents IFN type-I triggering by pestiviral single- and double-stranded RNAs. Virus Res. *140*, 15–23.

McCoy, A.J., Grosse-Kunstleve, R.W., Adams, P.D., Winn, M.D., Storoni, L.C., and Read, R.J. (2007). Phaser crystallographic software. J. Appl. Crystallogr. *40*, 658–674.

Meyer, C., Von Freyburg, M., Elbers, K., and Meyers, G. (2002). Recovery of virulent and RNase-negative attenuated type 2 bovine viral diarrhea viruses from infectious cDNA clones. J. Virol. *76*, 8494–8503.

Meyers, G., Saalmüller, A., and Büttner, M. (1999). Mutations abrogating the RNase activity in glycoprotein E(rns) of the pestivirus classical swine fever virus lead to virus attenuation. J. Virol. *73*, 10224–10235.

Modis, Y., Ogata, S., Clements, D., and Harrison, S.C. (2003). A ligand-binding pocket in the dengue virus envelope glycoprotein. Proc. Natl. Acad. Sci. USA *100*, 6986–6991.

Peterhans, E., and Schweizer, M. (2010). Pestiviruses: how to outmaneuver your hosts. Vet. Microbiol. *142*, 18–25.

Rostkowski, M., Olsson, M.H., Søndergaard, C.R., and Jensen, J.H. (2011). Graphical analysis of pH-dependent properties of proteins predicted using PROPKA. BMC Struct. Biol. *11*, 6.

Sali, A., and Blundell, T.L. (1993). Comparative protein modelling by satisfaction of spatial restraints. J. Mol. Biol. *234*, 779–815.

Schneider, R., Unger, G., Stark, R., Schneider-Scherzer, E., and Thiel, H. (1993). Identification of a structural glycoprotein of an RNA virus as a ribonuclease. Science *261*, 1169–1171.

Suzuki, A., Yao, M., Tanaka, I., Numata, T., Kikukawa, S., Yamasaki, N., and Kimura, M. (2000). Crystal structures of the ribonuclease MC1 from bitter gourd seeds, complexed with 2′-UMP or 3′-UMP, reveal structural basis for uridine specificity. Biochem. Biophys. Res. Commun. *275*, 572–576.

Tanaka, N., Arai, J., Inokuchi, N., Koyama, T., Ohgi, K., Irie, M., and Nakamura, K.T. (2000). Crystal structure of a plant ribonuclease, RNase LE. J. Mol. Biol. *298*, 859–873.

Tews, B.A., and Meyers, G. (2007). The pestivirus glycoprotein Erns is anchored in plane in the membrane via an amphipathic helix. J. Biol. Chem. *282*, 32730–32741.

Tews, B.A., Schürmann, E.-M., and Meyers, G. (2009). Mutation of cysteine 171 of pestivirus E rns RNase prevents homodimer formation and leads to attenuation of classical swine fever virus. J. Virol. *83*, 4823–4834.

Thiel, H.-J., Stark, R., Weiland, E., Rümenapf, T., and Meyers, G. (1991). Hog cholera virus: molecular composition of virions from a pestivirus. J. Virol. *65*, 4705–4712.

Trott, O., and Olson, A.J. (2010). AutoDock Vina: Improving the speed and accuracy of docking with a new scoring function, efficient optimization and multithreading. J. Comput. Chem. *31*, 455–561.

Vonrhein, C., Blanc, E., Roversi, P., and Bricogne, G. (2007). Automated structure solution with autoSHARP. Methods Mol. Biol. *364*, 215–230.

Wang, Z., Nie, Y., Wang, P., Ding, M., and Deng, H. (2004). Characterization of classical swine fever virus entry by using pseudotyped viruses: E1 and E2 are sufficient to mediate viral entry. Virology *330*, 332–341.

Weiland, E., Ahl, R., Stark, R., Weiland, F., and Thiel, H.J. (1992). A second envelope glycoprotein mediates neutralization of a pestivirus, hog cholera virus. J. Virol. *66*, 3677–3682.

Weiland, E., Stark, R., Haas, B., Rümenapf, T., Meyers, G., and Thiel, H.-J. (1990). Pestivirus glycoprotein which induces neutralizing antibodies forms part of a disulfide-linked heterodimer. J. Virol. *64*, 3563–3569.

Widjojoatmodjo, M.N., van Gennip, H.G., Bouma, A., van Rijn, P.A., and Moormann, R.J. (2000). Classical swine fever virus E(rns) deletion mutants: trans-complementation and potential use as nontransmissible, modified, live-attenuated marker vaccines. J. Virol. *74*, 2973–2980.

Windisch, J.M., Schneider, R., Stark, R., Weiland, E., Meyers, G., and Thiel, H.J. (1996). RNase of classical swine fever virus: biochemical characterization and inhibition by virus-neutralizing monoclonal antibodies. J. Virol. *70*, 352–358.